

Investigation on Dry Sliding Wear Performance and Corrosion Resistance of 13Cr5Ni2Mo Supermartensitic Stainless Steel

N.E. Beliardouh^{a,*}, S. Tlili^b, A. Oulabbas^{a,b}, C.E. Ramoul^{a,b}, S. Meddah^b, H. Kaleli^c

^aLaboratoire Ingénierie des Surfaces (LIS), Université Badji Mokhtar, BP 12, 23000, Annaba, Algeria,

^bResearch Center in Industrial Technologies CRTI P.O. Box 64, Cheraga 16014 Algiers, Algeria,

^cFaculty of Mechanical Engineering, Automotive Division, Yıldız Technical University, Istanbul, Turkey.

Keywords:

Supermartensitic steel
Microstructure
Friction
Wear
Corrosion

* Corresponding author:

Nasser Eddine Beliardouh 
E-mail: nebeliardouh23@gmail.com

Received: 26 September 2020

Revised: 27 October 2020

Accepted: 21 November 2020

ABSTRACT

This work aimed to study the microstructure, wear and corrosion resistance of supermartensitic stainless steel (SMSS). Heat treatment applied to samples consists of quenching after austenitization at elevated temperature (1250 °C) followed by a double tempering at 650 °C. Conventional mechanical properties, scanning electron microscopy (SEM/EDS) analysis and X-ray diffraction methods (XRD) are used to analyze the microstructure and to evaluate the wear mechanisms. The potentiodynamic polarisation and the electrochemical impedance spectroscopy (EIS) methods are used to evaluate the corrosion resistance in both the 0.5M H₂SO₄ and 0.5M NaCl aggressive media. The microstructure is mainly composed with tempered lath martensite, small quantity of retained austenite and carbides. Oxidative and abrasive wear dominated the wear process in dry condition. During the corrosion process, the same mechanism of degradation was found in both the 0.5M NaCl and 0.5M H₂SO₄.

© 2020 Published by Faculty of Engineering

1. INTRODUCTION

Supermartensitic stainless steel (SMSS) were developed and used in applications that require good tensile, deformation and fatigue strength properties in combination with corrosion and wear resistance. They are commonly used in oil and gas industries, particularly in the manufacturing of pipes[1]. During oil exploitation, the external parts of a pipe can be damaged by corrosion and wear. These failures

are dependent on the environment aggressiveness [2]. Under internal pressure conditions, the surface of a pipe at variable temperatures, is exposed to water, mud, soil, and possibly to sour environments [3].

The microstructure of SMSS, after thermal treatment at room temperature is generally, characterized by a mixture of tempered lath martensite and reversed austenite. The chemical composition of the SMSS is a key

factor influencing the final microstructure, the mechanical and chemical performances. Nickel stabilizes the low carbon austenite, Molybdenum is necessary to increase ductility and mechanical strength while chromium is well known as the essential element against corrosion. Elements such as Nb, Ti can be added to further increase the mechanical properties, through the MC carbide formation i.e. yield strength (Y.S), tensile strength, elongation and hardness. It was reported, that 0.1%Nb led to 30 % increase in Y.S [4]. In the same way but through another mechanism, the addition of a small amount of B can significantly enhance the hardenability [5]. The reason has been frequently attributed to the segregation of B at prior austenite grain boundaries.

Thermal treatment is the second way to obtain a compromise between mechanical properties, tribology, and resistance against corrosion. Heat treatment parameters must be chosen carefully such as austenitizing temperature, time, and cooling speed to ensure complete martensitic transformation and to avoid carbide precipitation and δ - ferrite formation during cooling stages [6-8]. The ideal microstructure will possess combination of strength, ductility, toughness and hardness i.e. hard enough to resist against abrasion as well as it will be ductile to absorb shock energy and no strong intergranular carbides to avoid corrosion (sensitization).

Hundreds of tons of SMSS, in the form of seamless tubes (old stock and scrap) are abandoned by oil companies because of their limited performance in aggressive environments such as the Algerian desert (Sahara). Recycling this material is of great importance, both from an economic point of view and in terms of environmental respect. Therefore, the goal was to explore the possibility to use SMSS material for other industrial applications than petroleum industry such as hot working dies and tools, propellers, pump impellers, ball bearings and races, bushings, valve seats, industrial knives [9], and parts of machines that work in agriculture, public works and building.

The scope of this current work is an attempt to solve a recycling problem i.e. recovery of SMSS pieces material based on adequate thermal treatments. Besides, to our knowledge, no data

about the tribological contact studied here were reported in the literature so far.

2. MATERIALS AND METHODS

2.1 Thermal treatments

Samples were cut from the transversal cross-section of a commercial seamless tube (13Cr5Ni2Mo specification), in the annealed condition as provided by the manufacturer. The chemical composition, listed in Table 1, was determined by X-ray fluorescence technique (XRF) and infrared spectroscopy (IRS).

Table 1. Chemical composition of the SMSS specimen in weight % (Fe as the balance).

Sample	Chemical composition [%]				
	C	Mn	Si	P	S
13Cr5Ni2Mo	0.018	0.411	0.215	0.011	0.004
	Cr	Ni	Cu	Mo	Fe
	12.25	5.45	0.245	2.06	bal

Charpy V-notch specimens with dimensions of 55 mm x 10 mm x 5 mm and tensile specimens (flat test specimen with dimensions of Overall length (L1) =300 mm, Width (b) = 20 mm, thickness (e) = 6 mm and the gage length (L2) =90 mm), were machined to undergo heat treatments before tests and analyses. Thermal treatments of the samples consisted of austenitization i.e. heating the virgin microstructure to 850 °C at a rate of 40 °C/min and maintained during 30 min for homogenization the temperature, thus homogenization the structural transformations (α -ferrite to γ -austenite). Then, an increase to the final isothermal level (1250 °C, 120 min) at a rate of 80 °C/min. The quenching process was performed in an oil bath (ambient temperature). This step guaranteed almost total martensitic transformation, minimum of retained austenite and crack risk formation. Immediately after that, specimens were held at a constant temperature of 650 °C, 120 min then ambient air-cooling. The latest process, repeated twice is called double tempering. The focus was (i) to permit the structural transformation into tempered martensite phase and to obtain the optimum combination between mechanical resistance, toughness, and elongation [10] (ii) to eliminate a

maximum of residual stresses and best second phases (carbides) precipitations i.e. homogeneous distribution in all the volume. These cycles of heat treatments (temperatures, times) are chosen based on a series of experiments performed previously in the laboratory. They give the best mechanical parameters (tensile properties, hardness). The thermal treatments are performed in a horizontal tube furnace under a protective argon flow atmosphere.

2.2 Microstructural analyses and mechanical properties

Polishing samples was performed gradually from Grid 180 SiC paper to final diamond dough (0.25 μm). After that, specimens were ultrasonically cleaned, dried in air, and etched for 4 minutes in the Vilella attack (1g picric acid + 10 ml hydrochloric acid + 100 ml ethanol). Finally samples are examined by ZEISS-EVO MA scanning electron microscope. The X-ray diffraction (XRD) analysis has been carried out by means of RIGAKU Ultima IV diffractometer using Cu K α radiation in the range of 2θ from 30 to 120°.

Hardness (H) and elastic parameters (E, ν) are obtained from the micro indentation technique using a Zwick/Roell Z2.5 machine (50N). The tensile-testing machine Zwick Z1200 and Zwick RPK 350 pendulum machine are used for mechanical properties determination (elongation, strength resistance).

2.3 Tribological tests

Tribological tests were carried out using a ball-on-disk tribometer (CSM Instrument NT1100) with automatic data acquisition system. The antagonist pair was the SMSS sample (20x20x4 mm; Ra= 0.06 \pm 0.01 μm) against alumina ball (H=13 GPa, provided by CSM Instrument) as a counterface under dry conditions. In order to simplify the geometry (calculation of maximum Hertzian contact pressure, wear volume) a spherical tips are frequently used; that is why a spherical pin was used in this study.

Sliding speed and applied load are among major factors that give high impact to the friction force and wear value [11]. In this work, the linear speed of 0.02 cm/s was kept constant for all of the experiments. However, three (03) load values

(2, 6 and 10 N) are tested for a total sliding distance of 20 m. All tests were run at room temperature (20-25 °C) and ~40-50 % humidity. Each test was repeated, at least, 3 times.

The wear volume was evaluated by measuring the 2D surface profile multiplying by the circumference of the wear track using Cyber-Technologies 3D-CT100 laser profilometer. The specific wear rate (Ws) was calculated according to the conventional formulas.

Tests performed under 6 and 10 N are chosen in order to determine how much is the maximum resistance of the material against plastic deformation under such severe conditions of sliding wear. The Hertzian max pressure values are 0.932, 1.345, and 1.595 GPa at 2, 6, and 10 N of applied load respectively.

2.3 Electrochemical analysis

The electrochemical behavior was investigated at room temperature (25 °C), in two aggressive solutions i.e. 0.5M NaCl and 0.5M H₂SO₄. Potentiodynamic polarization test and Electrochemical Impedance Spectroscopy (EIS) were performed using an Autolab 302 potentiostat-galvanostat conventional three-electrode cell with the sample as the working electrode, an Ag/AgCl electrode as the reference electrode, and platinum electrode as the counter electrode.

Before all the tests, samples were immersed in the electrolyte for 60 min to establish the steady-state potential. In these experiments, the working electrode surface was of 0.5 cm². A scanning rate of 1.0 mV.s⁻¹ was applied during the potentiodynamic polarization experiment. In the EIS measurement, a sinusoidal a.c perturbation of 5 mV amplitude was applied to the electrode at its corrosion potential (E_{corr}). The impedance data were collected over a frequency range of 100 kHz to 10 mHz.

3. RESULTS AND DISCUSSION

3.1 Microstructure and mechanical properties

Figure 1 shows results of the microstructural analyses. Figure 1a displays the X-ray spectrum obtained from SMSS specimen as heat treated.

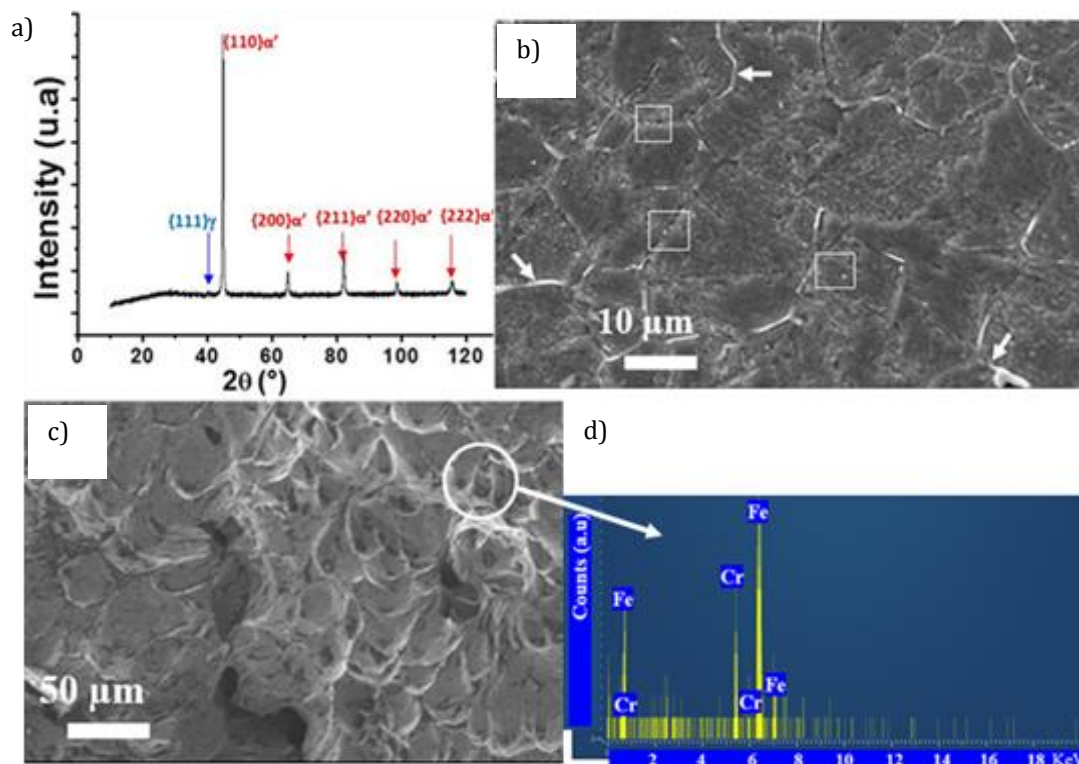


Fig.1. Microstructural analysis of the SMSS specimens (a) X-ray diffraction pattern (b) SEM image of the heat treatment microstructure: Tempered martensite, retained austenite (white arrows) and particles in squares (c) Rupture facies on broken Charpy impact sample at 21 °C and (d) EDS spectrum from circled zone in (c).

One can see that only two (2) crystalline phases are shown. Peaks located at $2\theta = 45^\circ(110)$, $65^\circ(200)$, $83^\circ(211)$, $99^\circ(220)$ and $115^\circ(220)$ correspond to the α' -martensite phase [12]. Only one peak, located at $2\theta = 40.1^\circ$ corresponds to $(111)\gamma$ -austenite phase. The $(200)\gamma$, $(220)\gamma$, and $(311)\gamma$ peaks are not visible because of their low intensity when compared to peak intensities of the α' martensite as this phenomenon has been encountered by several authors [10,13]. The amount of retained austenite was too low for a quantitative determination of its volume fraction. No other precipitates have been identified by the XRD characterization. Therefore, the microstructure seems to be fully martensitic with small amount of retained austenite. Figure 1b shows SEM micrograph of the final microstructure. It reveals fine martensitic lath matrix, a retained austenitic network along PAGs boundaries (Prior Austenite Grains) and globular precipitates (Fig. 1b).

In this field of material, PAGBs are sites of several segregations and precipitations [5]. On other hand, it is hard to distinguish PAGBs from other types of grain boundaries, such as block, packet boundaries or lath boundaries in

martensite. Therefore, one can say that is acceptable that retained martensite phase is only located at PAGBs.

Figure 1c shows the rupture facies of the SMSS at room temperature. It reveals ductile failure behavior of the microstructure at ambient temperature. The impact energy values measured at 21 and 80 °C are in the range of 166 ± 6 J. The Failure analysis of the specimens displays a dimpled surface with a fibrous fracture. The fracture appearance is rough, fibrous and torn. They are characteristics of appearance of a ductile fracture [14] i.e. appearance of yielding and plastic deformation. Figure 1c also reveals precipitates (circled area). These precipitates are most probably carbides as indicates by the presence of carburigen elements such as Fe and Cr elements in the EDS spectrum (Figure 1d). They are may be undissolved carbides (from virgin microstructure) otherwise they would have been precipitated during, or after heat treatments (secondary carbides). The stoichiometry of these carbides may be a MC or a M_23C_6 ($M = Mo, Cr, Fe$) type as reported by several authors [15-16]. No other precipitates were revealed by SEM analysis in this study.

Finally, the microstructure is principally constituted by bcc martensite (α') matrix (tempered martensite), a small quantity of retained austenite located in PAGs, and carbides. The SMSS investigated in this work presents best deformation capacity and comparable ductility with that reported by Mesquita *et al.* [17]. The range of hardness is 280 ± 5 Hv. The yield strength and tensile strength are found to be $(850 \pm 2$ MPa) and $(950 \pm 2$ MPa) respectively. The elongation reaches 20 %, done by tensile tests. The Young's Modulus is 203 ± 6 GPa.

3.2 Sliding wear study

Coefficient of Friction (COF)

Figure 2 shows the coefficient of friction evolution at different loads against alumina ball in dry condition. One can see the similar curves tendencies characterized by two steps; the first one is a short run-in which depends on the normal load intensity as clearly seen in Fig. 2 (vertical narrow); the run-in period decreases as the applied load increase.

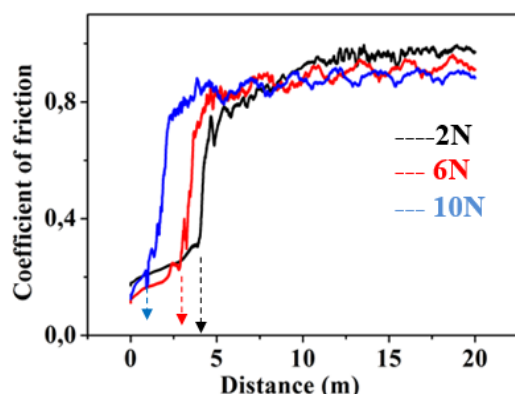


Fig. 2. The COF evolution of the SMSS specimens under dry conditions.

The second step starts after an abrupt increase of COF to higher values. Overall, the average values of the COF can be estimated at around 0.8 for the entire tested specimen whatever the applied load. Automatic values given by the system, at the steady state are 0.771, 0.765, and 0.806 at 2, 6 and 10 N respectively. The run-in period (first stage) corresponds to the contact between hard asperities of alumina ball rubbing against SMSS surface. Therefore, it undergoes a soft abrasive wear (polishing wear). After that, the friction force increases because of the abrasion. Alumina ball is considered as an inert counter body, so no chemical interaction between antagonists should be expected.

Wear mechanism analysis

Figure 3a shows wear tracks after tribo-test in dry condition of the SMSS at different applied normal loads. Figure 3b, corresponds to wear track tested under 2 N of applied load. It can be seen that the surface damages are typical of abrasive wear with grooves aligned in the rotation direction (label 1 in Fig. 3c). The worn surface showed a relatively rough the wear track with a small holes and few quantity of material removal (debris). The damage was mostly due to the formation of an oxide layer (tribo-chemical reaction). After a number of sliding cycles, this surface layer becomes brittle and transformed into debris. Figures 3b-3c, clearly indicated delamination areas of this oxide layer (label 2). Therefore, the sample has undergone an oxidative wear followed by soft third body abrasive wear.

Damages are more pronounced in the case of 6 N and 10 N due to the higher contact pressure as expected (Figs. 4a-4d).

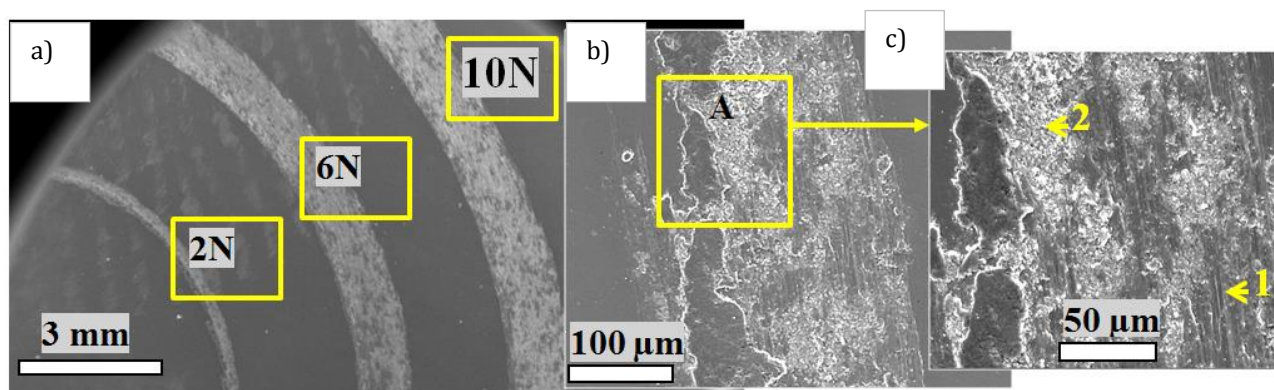


Fig. 3. SEM micrographs of wear tracks, after tribotest of the SMSS specimens (a) general view of wear tracks on the tested sample (b) wear track corresponding to 2N of applied load (c) zoom of the square A (1- groove, 2- delaminated area).

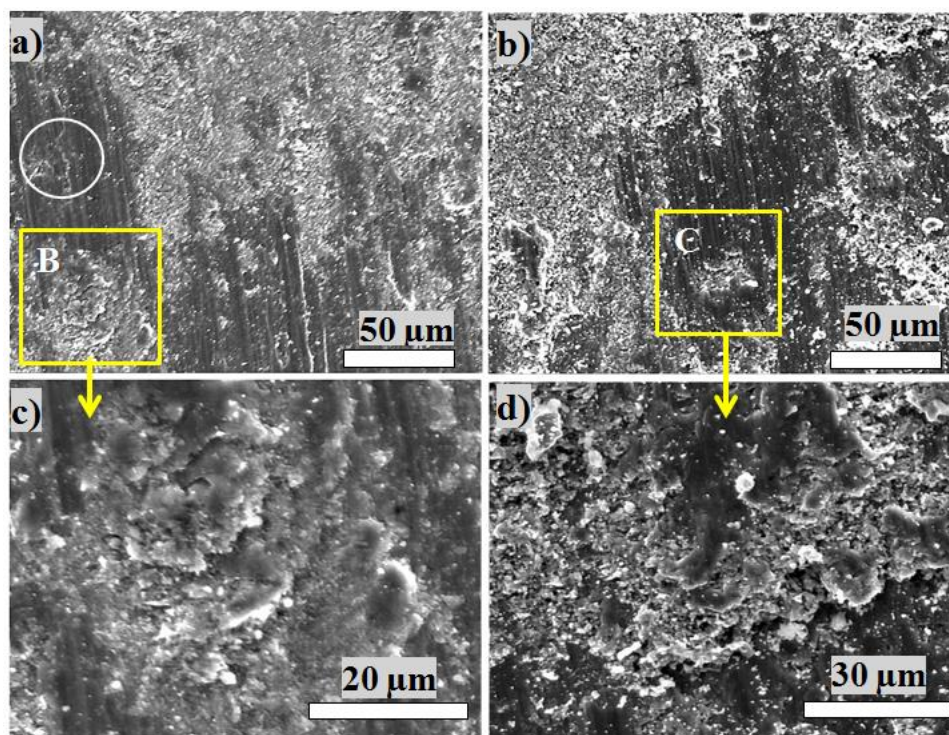


Fig. 4. SEM micrographs of the wear tracks of the SMSS specimens after tribo-tests (a) at 6 N and (b) at 10 N of applied load; (c) and (d) high magnification images of squares B and C respectively; spalling phenomena of the tribo-layer formation.

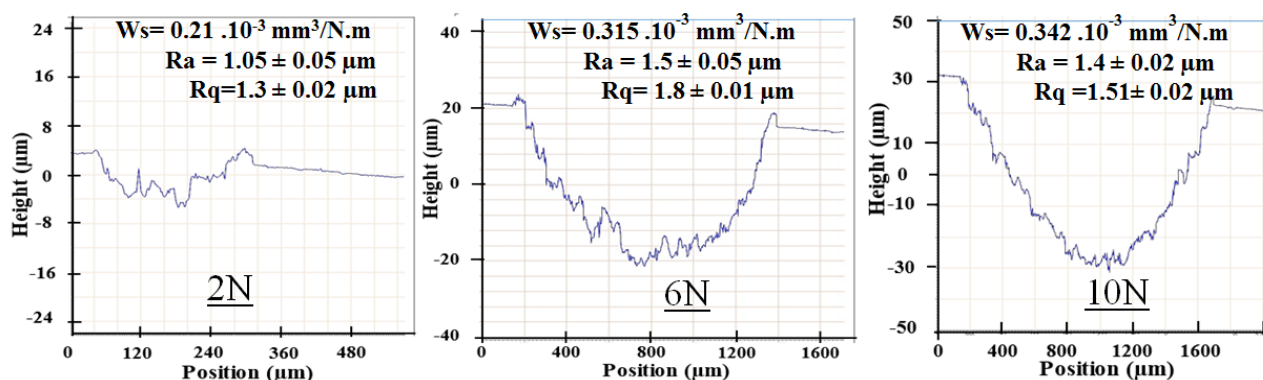


Fig. 5. Effect of applied load on 2D profile of wear tracks of the SMSS specimens.

The SEM images revealed the formation of grooves running parallel to the sliding direction, plastic deformation, relatively high amount of material removal, holes, and craters (circled area). A clear evidence of a severe abrasive wear was shown. The contact zone (track) exhibited spalling (Figs. 4c-4d) and much more accumulated materials over the wear track.

The detachment of small particles e.g. carbides, from the martensitic matrix material, is the origin of holes in abrasive wear. However, the same mechanisms, observed in the last case (2 N), are evolved during the sliding process. Rubbing the disc against alumina ball led to an

increase in temperature thus to an oxide layer formation. The latest, after more and more cycles of sliding becomes brittle (unstable) leading to the spalling phenomena, after that to wear debris formation.

Finally, formation of grooves and ridges running parallel to the sliding direction are the common features at both lower and higher loads and the tribo-layer formation was the main mechanism that controls the wear process.

Figure 5 shows examples of a 2D profiles taken from wear tracks of tribo-tested specimens. It obviously shows that the wear rate ($W_s \pm 0.03 \text{ mm}^3/\text{Nm}$) of the SMSS specimens enhances

with an increase in load. Specific wear rate results, in Fig. 5, also confirm SEM analysis; it indicated that the low worn volume (volume loss) was found at 2N of the applied load. In the same way, as the applied load increases, the roughness parameters, (R_a =arithmetic average, R_q =Root-mean-square) within the wear tracks, increase.

3.3 Corrosion behavior

Figure 6 illustrates the polarization curves of samples recorded in both 0.5M NaCl and 0.5M H₂SO₄. Generally, the cathodic region of the polarization curve describes the cathodic hydrogen evolution reaction associated with water reduction. The anodic part of the polarization curve represents the dissolution of the sample at an elevated potential. The corrosion current densities (I_{corr}) were calculated by means of Tafel extrapolation i.e. extrapolation of linear parts of anodic and cathodic curves to the point of convergence of the relating corrosion potential [18].

The curves showed very similar profiles as can be seen from Fig. 6a. One can observe that all curves present similar behavior. However, the best polarization resistance of the samples should be expected in 0.5M NaCl. The corrosion potential vs. Ag/AgCl (E_{corr})_{Ag/AgCl} and (I_{corr}) in 0.5M NaCl are -335 mV and 0.015 mA/cm² respectively. While, in 0.5M H₂SO₄, (I_{corr}) is equal to 0.027 mA/cm² (i.e. highest by a factor ~ 2, in comparison with I_{corr} in 0.5M H₂SO₄) and the (E_{corr})_{Ag/AgCl} is equal to -328.2 mV.

Potentiodynamic results have been complemented by EIS analysis. Indeed, EIS is a very powerful technique to electrochemically characterize the properties and behavior of film formation.

Figure 6b, shows representative EIS curves in Nyquist diagram. The EIS spectra of both immersed samples in NaCl and H₂SO₄ are characterized by two well defined loops; a capacitive loop in the high frequency (HF) region and a second capacitive loop in the low frequency region (LF). The first one in the HF region is associated with the charge transfer resistance (R_{ct}). This is because of the resistance during electron transfer in parallel to the double layer capacitance (CPE_{dl}) at the interface between the surface of the metal and the aggressive medium. While the second capacitive loop (LF) is attributed to the diffusion in solid process i.e. the mass transport through the corrosion product layer (R_c , CPE_c). Consequently two capacitive behaviors occurred for the entire tested specimens. A larger diameter loop equates to higher corrosion resistance. By comparing the diameters of the loops in the Nyquist plot, the sample's corrosion properties can be easily evaluated.

Figure 6c indicates the selected electrical equivalent circuit model (EEC), generally used in neutral and sulfate acidic media, to fit EIS results. The (EEC) model consists with electrolyte resistance R_e (0.5M NaCl and/or 0.5M H₂SO₄). R_{ct} and CPE_{dl} are resistance and capacitance corresponding to the loop at HF in Nyquist diagram while R_c and CPE_c correspond to the second loop at LF in Nyquist diagram (Fig. 6b).

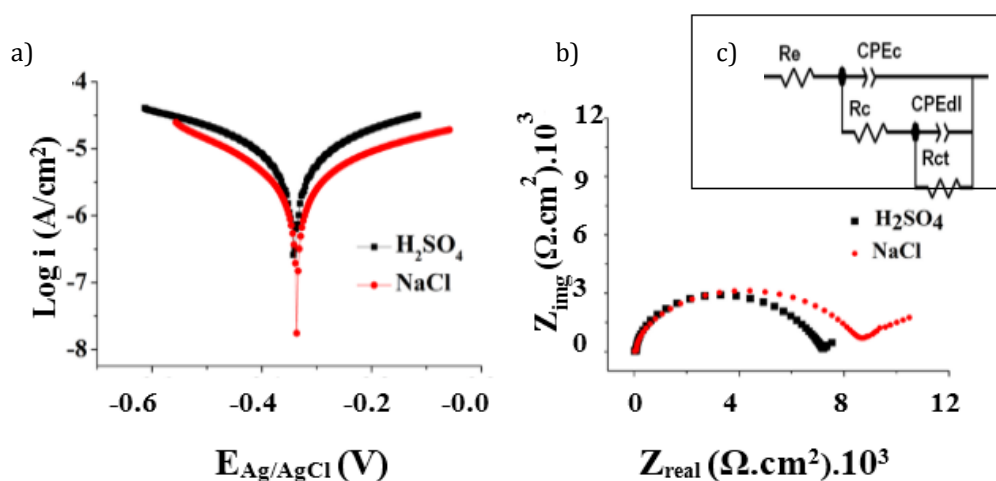


Fig. 6. Electrochemical test results of the SMSS specimens; (a) potentiodynamic polarization curves (b) Nyquist plots of SMSS samples recorded after immersion in 0.5M NaCl and 0.5M H₂SO₄ solutions and (c) the equivalent electrical circuit (EC) used for analysis of EIS spectra.

Table 2. EIS fitted results for spectra obtained from tested SMSS specimens.

Electrolyte	Re ($\Omega \text{ cm}^{-2}$)	CPE _{dl} ($F.S^{1/n}$).10 ⁻⁶	R _{ct} ($\Omega \text{ cm}^{-2}$)	CPE _c ($F.S^{1/n}$).10 ⁻⁹	R _c ($\Omega \text{ cm}^{-2}$).10 ⁺³
0.5M NaCl	6.96	5.96	140	102	9.13
0.5M H ₂ SO ₄	34.3	3.97	1310	115	5.97

Table 2 presents a quantitative analysis of EIS data by fitting the appropriate electrical equivalent circuit (EEC) determined from the Nyquist plots using the *Ec Lab software*. The EEC model with two loop elements, as shown in Fig. 6c produced a good fit on the impedance data for SMSS samples. Results from table 2 indicate that the SMSS sample has the highest resistance of polarization ($R_p = R_c + R_{ct}$) of $9.27 \text{ k}\Omega \text{ cm}^{-2}$ when against Cl⁻. This means that SMSS material opposes much more resistance because Cl⁻ can penetrate through intergranular boundaries, migrate to the metal/oxide interface, and reach the metal surface, resulting in fracture of the passive film.

Nyquist plots presented in Fig. 6b, confirm the observations taken from polarization curves (Fig. 6a) and Table 2.

Finally, small corrosion current density, large resistance, big impedance, implies that SMSS shows acceptable resistance in both the acidic and neutral solutions.

This experimental work was done to corroborate the obtained microstructure of industrial SMSS seamless tube, with various performances in terms of wear resistance against hard matter (alumina ball) and corrosion in both acidic and neutral media. Results were discussed in light of the mechanisms through which wear and corrosion susceptibility correlates with crystalline phases formed after the thermal treatment i.e. austenitization and subsequent cooling followed by double tempering.

As mentioned above, microstructural analyses (SEM/EDS and XRD) indicated both the presence of martensite matrix, retained austenite, and carbide precipitation. These results are in agreement with cited articles. The hardness value found in this work ($280 \pm 5 \text{ HV}$) is in the hardness range, expected for SMSS materials i.e. 260 to 310 HV [19]. This value reflects both the contribution of the martensite matrix and precipitates. The high density of dislocations

induced by the martensitic transformation has led to a stressed structure thus to a high hardness. After that, hardness will be decreased during tempering because of the microstructure softening due to the massive elimination of dislocations. Mechanical properties are taken from conventional tests (tensile and Charpy impact tests). They reflect the microstructure's effect and confirm a recent work reported by Jun He *et al.* [20]. It was established, on one hand, the refinement of the prior austenite grain size has a great influence on the size of the martensitic laths (packet size) [21]. On the other hand, the SMSS gained strength from intragranular precipitation inside the martensite matrix e.g. carbides (the case of this work Figs. 1c-1d) and intermetallic precipitations [22] since it contains more than four metallic elements. Thus, the choice of the treatment's parameters (time, temperature) seems to be adequate.

The microstructure influences the tribological behavior in terms of coefficient of friction, specific wear rate, and wear mechanisms involved during dry sliding wear. From the results obtained here (Figs. 2 to 5), the sample has undergone oxidative wear followed by soft third body abrasive wear at low normal load. An increase in the applied load (increase in contact pressure) leads to severe abrasive wear in addition to adhesive wear. Obtained findings are in good agreement with the literature reviewed so far [9]. The abrasiveness of the precipitated particles during tempering (intermetallic particles, oxides, carbides...) is among factors influencing deeply the wear rate. Therefore, minimizing the wear damages requires adequate surface microstructure i.e. finest γ -austenite grains leading to finest martensite lath packets in addition to finest precipitates homogeneously dispersed in the matrix.

To simplify the discussion, it is believed that, for improved corrosion resistance of stainless steel, a single-phase microstructure is more attractive than a multiphase because of the probable formation of galvanic microcells between the various microstructural phases. This could be

the case when different metallurgical phases are in direct electrical contact e.g. at matrix/precipitate interface. Unfortunately, such a single microstructure is not easily realizable in the present case of industrial SMSS material. Following the results it can be stated, that both the potentiodynamic and EIS methods indicate a slightly better corrosion resistance, when against chloride ions. Indeed, the corrosion potential values (NaCl or H₂SO₄) are approximately in the same range, while the highest current density was found in the acidic solution. EIS results indicated that the surface itself affords the best corrosion protection due to the stability of the passive film.

4. CONCLUSIONS

In the present work, the dry wear of 13Cr5Ni2Mo steel against alumina ball and the corrosion resistance in both alkaline and acidic solutions were evaluated. The following conclusions can be drawn as follows:

- The microstructure was characterized by a dense martensitic matrix, low content of retained austenite, and carbides.
- Increasing in applied load led to an increase in wear volume and transforms the wear mechanism (from a soft abrasive wear to a severe abrasive wear).
- The electrochemical studies, evaluated based on potentiodynamic and SIE methods show that the highest corrosion resistance of the tested specimen occurs in the 0.5M H₂SO₄.
- The thermal treatment, tested in this work, provides acceptable mechanical properties to the SMSS samples and allows them to be recycled and suitable for the manufacture of equipment for industries other than oil and petroleum companies.

Acknowledgement

The authors are grateful to the Directorate General For Scientific Research and Technological Development (DGRSDT) at the Algerian Ministry of Higher Education and Scientific Research (MESRS) for its support.

REFERENCES

- [1] G. Zepon, C.S. Kiminami, W.J. Botta Filho, C. Bolfarini, *Microstructure and Wear Resistance of Spray-formed Supermartensitic Stainless Steel*, Materials Research, vol. 16, no. 3, pp. 642-646, 2013, doi: [10.1590/S1516-14392013005000026](https://doi.org/10.1590/S1516-14392013005000026)
- [2] G.A. Rodríguez-Bravo, M. Vite-Torres, J.G. Godínez Salcedo, *Analysis on the Corrosion Rate Changes of AISI 410 Stainless Steel Submitted to Abrasion-Corrosion in Simulated Marine Conditions*, Proceedings on Engineering Sciences, vol. 1, no. 1, pp. 90-97, 2019, doi: [10.24874/pes01.01.012](https://doi.org/10.24874/pes01.01.012)
- [3] M. Monnot, R.P. Nogueira, V. Roche, G. Berthomé, E. Chauveau, R. Estevez, M. Mantel, *Sulfide Stress Corrosion Study of a Super Martensitic Stainless Steel in H₂S sour environments: Metallic Sulfides Formation and Hydrogen Embrittlement*, Applied Surface Science, vol. 394, pp. 132-141, 2016, doi: [10.1016/j.apsusc.2016.10.072](https://doi.org/10.1016/j.apsusc.2016.10.072)
- [4] X.P. Ma, L.J. Wang, C.M. Liu, S.V. Subramanian, *Role of Nb in Low Interstitial 13Cr Super Martensitic Stainless Steel*, Materials Science and Engineering: A, vol. 528, iss. 22-23, pp. 6812-6818, 2011, doi: [10.1016/j.msea.2011.05.065](https://doi.org/10.1016/j.msea.2011.05.065)
- [5] Y.J. Li, D. Ponge, P. Choi, D. Raabe, *Segregation of Boron at Prior Austenite Grain Boundaries in a Quenched Martensitic Steel Studied by Atom Probe Tomography*, Scripta Materialia, vol. 96, pp. 13-16, 2015, doi: [10.1016/j.scriptamat.2014.09.031](https://doi.org/10.1016/j.scriptamat.2014.09.031)
- [6] M.C. dos Santos Fernandes, S. Nakamatsu, S. Capellari De Rezende, S.C. Maestrelli, L.L. de Sousa, N.A. Mariano, *Tempering Temperature Influence on 13Cr4Ni0.02C Steel Corrosion Resistance*, Materials Research, vol. 20, iss. 2, pp. 537-542, 2017, doi: [10.1590/1980-5373-mr-2017-0026](https://doi.org/10.1590/1980-5373-mr-2017-0026)
- [7] Y. Zhang, C. Zhang, X. Yuan, D. Li, Y. Yin, S. Li, *Microstructure evolution and orientation relationship of reverted austenite in 13Cr Supermartensitic Stainless Steel During the Tempering Process*, Materials, vol. 12, iss. 4, pp. 589-602, 2019, doi: [10.3390/ma12040589](https://doi.org/10.3390/ma12040589)
- [8] L. Bacchi F. Biagini, S. Corsinovi, M. Romanelli, M. Villa, R. Valentini, *Influence of Thermal Treatment on SCC and HE Susceptibility of Supermartensitic Stainless Steel 16Cr5NiMo*, Materials, vol. 13, iss. 7, pp. 1643- 1657, 2020, doi: [10.3390/ma13071643](https://doi.org/10.3390/ma13071643)
- [9] A. Dalmau, C. Richard, A. Igual-Muñoz, *Degradation Mechanisms in Martensitic Stainless Steels: Wear, Corrosion and Tribocorrosion Appraisal*, Tribology International, vol. 121, pp. 167-179, 2018, doi: [10.1016/j.triboint.2018.01.036](https://doi.org/10.1016/j.triboint.2018.01.036)

- [10] M.P. de Oliveira, J.W. Calderon-Hernandez, R. Magnabosco, D. Hincapie-Latino, N. Alonso-Falleiros, *Effect of Niobium on Phase Transformations, Mechanical Properties and Corrosion of Supermartensitic Stainless Steel*, Journal of Material Engineering and Performance, vol. 26, pp. 1664-1672, 2017, doi: [10.1007/s11665-017-2610-1](https://doi.org/10.1007/s11665-017-2610-1)
- [11] N. Nuraliza, S. Syahrullail, M.H. Faizal. *Tribological Properties of Aluminum Lubricated With Palm Olein at Different Load using Pin-on-disk Machine*, Journal Tribologi, vol. 9, pp. 45-59, 2016.
- [12] A. Bojack, L. Zhao, P.F. Morris, J. Sietsma, *In-situ Determination of Austenite and Martensite Formation in 13Cr6Ni2Mo Supermartensitic Stainless Steel*, Materials Characterization, vol. 71, pp. 77-86, 2012, doi: [10.1016/j.matchar.2012.06.004](https://doi.org/10.1016/j.matchar.2012.06.004)
- [13] R.B. Soares, L.F. Pinheiro Dick, S.M. Manhalbosco, A.P. dos Santos, W.R. Da Costa Campos, J.D. Aedisson, V. de Freitas Cunha Lins, *Metallurgical and Electrochemical characterization of a Supermartensitic Steel*, Materials Research, vol. 23, no. 2, 2020, doi: [10.1590/1980-5373-mr-2019-0280](https://doi.org/10.1590/1980-5373-mr-2019-0280)
- [14] A. Waqas, X. Qin, J. Xiong, C. Zheng, H. Wang, *Analysis of Ductile Fracture Obtained by Charpy Impact Test of a Steel Structure Created by Robot-Assisted GMAW-Based Additive Manufacturing*, Metals, vol. 9, iss. 11, p. 1208, 2019, doi: [10.3390/met9111208](https://doi.org/10.3390/met9111208)
- [15] I. Yu Pyshmintsev, S.M. Bitjukov, V.I. Pastukhov, S.V. Danilov, L.O. Vedernikova, M.L. Lobanov, *Evolution of Microstructure Stainless Martensitic Steel for Seamless Tubing*, AIP Conference Proceedings, vol. 1915, 2017, doi: [10.1063/1.5017396](https://doi.org/10.1063/1.5017396)
- [16] S. Hollner, B. Fournier, J. Le Pendu, T. Cozzika, I. Tournié, J.-C. Brachet, A. Pineau, *High-temperature Mechanical Properties Improvement on Modified 9Cr-1Mo Martensitic Steel Through Thermomechanical Treatments?* Journal of Nuclear Materials, vol. 405, iss. 2, pp. 101-108, 2010, doi: [10.1016/j.jnucmat.2010.07.034](https://doi.org/10.1016/j.jnucmat.2010.07.034)
- [17] T.J. Mesquita, E. Chauveau, M. Mantel, N. Bouvier, D. Koschel, *Corrosion and Metallurgical Investigation of two Supermartensitic Stainless Steels for Oil and Gas Environments*, Corrosion Science, vol. 81, pp. 152-161, 2014, doi: [10.1016/j.corsci.2013.12.015](https://doi.org/10.1016/j.corsci.2013.12.015)
- [18] Metals Handbook Corrosion: *Fundamentals, Testing and Protection*, 9th ed., vol. 13A, 2003.
- [19] C.A.D. Rodrigues, R.M. Bendeira, B.B. Duarte, G. Tremiliosi-Filho, V. Roche, A.M. Jorge Jr, *Effect of Titanium Nitride (TiN) on the Corrosion Behavior of a Supermartensitic Stainless Steel*, Materials and Corrosion, vol. 70, iss. 1, pp. 28-36, 2019, doi: [10.1002/maco.201810289](https://doi.org/10.1002/maco.201810289)
- [20] J. He, L. Chen, X. Tao, S. Antonov, Y. Zhong, Y. Su, *Hydrogen Embrittlement Behavior of 13Cr-5Ni-2Mo Supermartensitic Stainless Steel*, Corrosion Science, vol. 176, 2020, doi: [10.1016/j.corsci.2020.109046](https://doi.org/10.1016/j.corsci.2020.109046)
- [21] C. Wang, M. Wang, J. Shie, W. Hui, H. Dang, *Effect of Microstructural Refinement on the Toughness of Low Carbon Martensitic Steel*, Scripta Materialia, vol. 58, iss. 6, pp. 492-495, 2008, doi: [10.1016/j.scriptamat.2007.10.053](https://doi.org/10.1016/j.scriptamat.2007.10.053)
- [22] S.D. Meshram, G.M. Reddy, S. Pandey, *Friction Stir Welding of Maraging Steel (Grade-250)*, Material & Design, vol. 49, pp. 58-64, 2013, doi: [10.1016/j.matdes.2013.01.016](https://doi.org/10.1016/j.matdes.2013.01.016)